



Three-dimensional nanoporous TiO₂ network films with excellent electrochemical capacitance performance



Huan Zhou, Yuan Zhong, Zhishun He, Liying Zhang, Jianming Wang*, Jianqing Zhang, Chu-nan Cao

Department of Chemistry, Zhejiang University, Hangzhou 310027, PR China

ARTICLE INFO

Article history:

Received 29 December 2013
Received in revised form 28 January 2014
Accepted 28 January 2014
Available online 6 February 2014

Keywords:

Titanium dioxide
Nanoporous structure
Hydrogenation
Supercapacitor
Dealloying

ABSTRACT

The three-dimensional (3D) nanoporous hydrogenated TiO₂ (denoted as H-TiO₂) network film on titanium substrate was fabricated by a novel and controllable method. The fabrication process involved dealloying, alkaline reflux and hydrogenation. The dealloying produced the 3D nanoporous titanium film with open pores and interconnected nanoflakes nearly perpendicular to the substrate. The oxidation of the 2D titanium nanoflakes in the alkaline reflux resulted in the formation of the TiO₂ nanotubes with an inner diameter of 5–10 nm and a length larger than 1.5 μm. The 3D nanoporous TiO₂ network film was formed by the self assembly of these long and thin TiO₂ nanotubes. Hydrogenation induced the formation of oxygen vacancies and more hydroxyl groups on the H-TiO₂ surface. The 3D nanoporous H-TiO₂ network film presented a capacitance of 1.05 mF cm⁻² at the scanning rate of 100 mV s⁻¹. Furthermore, the H-TiO₂ network film electrode also showed remarkable rate capability as well as excellent electrochemical cycling stability with a capacitance reduction of less than 7% after 1000 charge–discharge cycles at the current density of 100 μA cm⁻². The prominent electrochemical capacitance properties of the 3D H-TiO₂ network film electrode could be attributed to its unique structural characteristics.

© 2014 Elsevier B.V. All rights reserved.

1. Introduction

Electrochemical capacitors (ECs), also called supercapacitors or ultracapacitors, are regarded as promising power sources for hybrid electric vehicles and portable electronic devices due to their long cycle life and great power densities [1–6]. In general, based on their charging mechanisms, ECs fall into two categories, electrochemical double layer capacitor (EDLC) and pseudocapacitors. The former is based on the separation of charges at the interface between the electrode and electrolyte. The latter utilizes the fast faradic process involving reversible redox reactions [3].

Over the past decade, numerous substances have been explored as possible supercapacitor electrode materials such as carbonaceous materials [7], conducting polymers [8], hybrid composites and transition metal oxides [9]. In recent years, more attention has been devoted to synthesis of nanoporous materials. Many investigations have demonstrated that the hierarchical structures with highly porous characteristics may improve the performances of materials [10–15]. To date, numerous 3D porous structured materials, such as VO₂ [16], MnO₂ [17], Co₃O₄ [18], Nb₂O₅ [19] and Ni(OH)₂ [20], have been intensively explored as supercapacitor

materials, and these studies have resulted in significant enhancement of capacitance storage. In all these cases, the controllable synthesis of 3D nanostructures plays an important role to achieve the application targets of advanced materials.

Titanium dioxide has been considered as a promising electrode material for supercapacitors because of its low cost, natural abundance, high chemical stability and environmental friendliness [21–23]. In general, TiO₂ contributes a very low non-faradic capacitance (10–40 μF cm⁻²) in the charge–discharge process [24–26]. It is widely believed that the low electrochemical capacitance results from the low specific surface area and high electric resistance of TiO₂. Various synthetic strategies [27–33] have been probed to improve the electrochemical capacitance of TiO₂. Ramadoss et al. [27] prepared vertically aligned TiO₂ nanorod arrays on fluorine doped tin oxide substrate using a hydrothermal method, and the as-prepared electrode exhibited a maximum specific capacitance of 85 μF cm⁻² at a scan rate of 5 mV s⁻¹ and a capacitance retention ratio of 80% after 1000 cycles. Salari et al. [28,33] found that the specific capacitance value (911 μF cm⁻²) of the TiO₂ nanotube array heat-treated under argon atmosphere was much higher than that (30 μF cm⁻²) of the corresponding TiO₂ sample heat-treated under air atmosphere. Recently, it was demonstrated that the donor densities and electrochemical activity of TiO₂ nanostructures can be significantly improved by the thermal treatment in

* Corresponding author. Tel.: +86 571 87951513; fax: +86 571 87951895.

E-mail address: wjm@zju.edu.cn (J. Wang).



Fig. 1. Schematic illustration for the fabrication process of three-dimensional (3D) nanoporous H-TiO₂ network film.

hydrogen atmosphere [34–36]. Although the above investigations have been conducted, the controllable fabrication of 3D nanoporous TiO₂ films with prominent electrochemical capacitance properties still remains a great challenge.

In this investigation, we report a novel strategy for the fabrication of a 3D nanoporous hydrogenated TiO₂ network film on titanium substrate, as illustrated in Fig. 1. Attractively, it is found that the 3D nanoporous network consists of thin TiO₂ nanotubes. The fabrication mainly includes dealloying, alkali reflux and annealing in hydrogen-containing atmosphere (hydrogenation). It is demonstrated that the as-prepared 3D nanoporous TiO₂ network film exhibits large specific capacitance, excellent rate capability and high electrochemical-cycling stability. The reasons that the 3D nanoporous TiO₂ network film shows prominent electrochemical capacitance performance are discussed in detail.

2. Experimental

2.1. Electrode preparation

The porous Ti film was first fabricated by a dealloying method. A zinc film was prepared by a cathodic electrodeposition in the electrolyte solution containing 0.6 M ZnSO₄, 0.1 M (NH₄)₂SO₄ and 10 mM sodium dodecyl sulfate (SDS) at room temperature. A titanium foil (99.5%, 1.0 cm × 2.0 cm × 0.25 mm, Alfa Aesar) was assembled as the working electrode. Prior to deposition, the titanium foil was polished with 2000# grit waterproof abrasive paper, and ultrasonically cleaned in acetone and deionized water for 10 min, respectively. The deposition was conducted in a two-electrode cell with a platinum counter electrode at a constant current density of 10 mA cm⁻² for 30 min. After rinsed extensively with deionized water and dried in a nitrogen stream, the titanium foil with the electrodeposited zinc layer was annealed at 150 °C for 2 h in an Ar-filled tube furnace. The selective dissolution of zinc from the annealed film was carried out in 1 M KOH solution at 60 °C for 10 h. The obtained porous Ti film was refluxed in a three-necked flask with 6 M KOH solution at 110 °C for 12 h. After the refluxing, the sample was washed in deionized water and immersed in 0.5 M hydrochloric acid for 12 h. After rinsed with deionized water and dried in a nitrogen stream, the resulting sample was annealed at 630 °C in air and the 20% hydrogen-containing argon for 2 h, respectively. In the following discussions, the samples annealed in air and the 20% hydrogen-containing argon were designated as air-TiO₂ and H-TiO₂, respectively.

2.2. Physical characterization

The X-ray diffraction (XRD) patterns of film electrodes were recorded using a Rigaku D/Max 2550 X-ray diffractometer with Cu Kα radiation at 40 kV and 300 mA. The X-ray photoelectron spectroscopy (XPS) analysis of film electrodes was performed by a PHI 5000C X-ray physical electronics photoelectron spectrometer with Mg Kα radiation at 15 kV and 500 W. The morphologies and microstructures of various film electrodes were observed with scanning electron microscopy (SEM, SIRION-100, FEI Co. Ltd.) and transmission electron microscopy (TEM/HRTEM, JEM-2010, JEOL), respectively. The surface composition of the Ti film was analyzed by energy dispersive X-ray (EDX) spectroscopy (GENE IS 4000).

2.3. Electrochemical measurements

Electrochemical measurements were performed at room temperature in a typical three-electrode glass cell with a platinum counter electrode and a Ag/AgCl reference electrode. Various film electrodes were used as the working electrode. 0.5 M Na₂SO₄ aqueous solution was employed as electrolyte. Cyclic voltammetry (CV) was measured at various scan rates using a potentiostat (CHI 660C). Electrochemical impedance spectroscopy (EIS) measurements were carried out by an electrochemical analyzer (Parstat 2273), with the frequency range of 100 kHz to 0.01 Hz and a.c. signal amplitude of 5 mV. Galvanostatic charge/discharge tests were performed at various current densities by a potentiostat (Arbin BT-2000, USA).

The average specific capacitance (C , F cm⁻²) from the CV curves is calculated according to the following integral equation (1). The average specific capacitance (C , F cm⁻²) from the charge/discharge curves can be calculated in terms of Eq. (2) [28].

$$C = \frac{1}{v \cdot \Delta V \cdot S} \int I_{(v)} dV \quad (1)$$

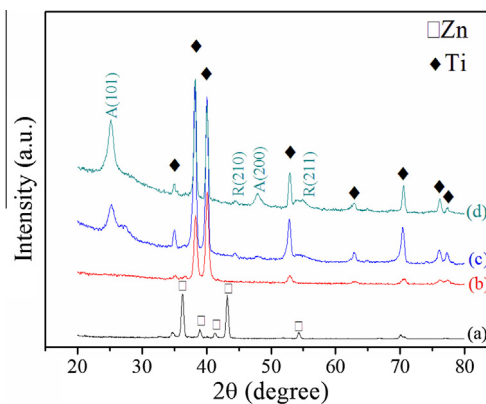


Fig. 2. XRD patterns of the annealed alloy film (a), dealloying film (b) and final product films annealed in air (c) and the hydrogen-containing argon (d). Symbols A and R represent anatase and rutile phases (JCPDS card no. 71-1166 and 89-6975), respectively.

$$C' = \frac{I \cdot \Delta t}{\Delta V \cdot S} \quad (2)$$

where S (cm²) is the geometric area of the working electrode, v (mV s⁻¹) is the potential scan rate, ΔV (V) is the sweep potential window, $I_{(v)}$ (A) is the voltammetric current on CV curves, I (A) is the applied current, and Δt (s) is the discharge time.

3. Results and discussion

Fig. 2 illustrates the XRD patterns of various films. As shown in Fig. 2a, the annealed alloy film consists of a mass of zinc (JCPDS card no. 65-3358) and a small quantity of titanium (JCPDS card no. 44-1294). The mutual diffusion of Zn and Ti during the heat treatment results in the formation of Zn–Ti alloy surface film, which is similar to the formation process of Zn–Ni alloy film [37]. The XRD pattern of the dealloying film in Fig. 2b shows that the XRD peaks of zinc disappear and the XRD peaks of Ti appear, indicating that the porous Ti film is obtained through the selective etching of zinc from the annealed film in the alkaline solution [37]. The EDX result in Fig. 3 reveals that a large amount of Ti and a small quantity of oxygen exist in the dealloying film, suggesting that titanium is covered with a thin oxide layer. As shown in

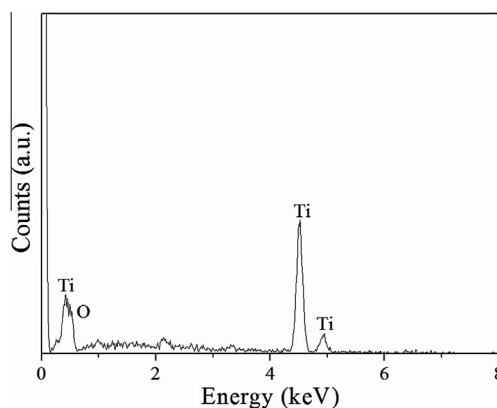


Fig. 3. EDX analysis of the dealloying film.

Fig. 2c and d, the final product films annealed in both air and the hydrogen-containing argon are composed of anatase and rutile phases of TiO_2 . That is, the hydrogenation treatment does not alter the phase structure of TiO_2 . The transformation from metallic Ti to Ti (IV) generally results from the oxidation of oxygen during the refluxing treatment. In energy storage applications such as batteries and supercapacitors, it has been demonstrated that the electrochemical properties of titania particles mostly depend on the particle size rather than the phases, and no significant differences are found between rutile and anatase [23,38].

The effect of hydrogenation on the chemical composition and oxidation state of the TiO_2 film was obtained from XPS measurements. Fig. 4a shows the XPS spectra of Ti 2p signal for H- TiO_2 and air- TiO_2 samples. The two peaks at 465.1 and 458.9 eV can be attributed to the characteristic Ti 2p_{1/2} and Ti 2p_{3/2} peaks [34,35], respectively. Compared to those of air- TiO_2 , the peaks of H- TiO_2 show a shift towards the lower binding energy. This indicates that the Ti atoms in two samples have different chemical environments, suggesting the existence of Ti^{3+} (oxygen vacancies) inside H- TiO_2 [36]. Fig. 4b and c compare the O 1s core level XPS spectra of air- TiO_2 and H- TiO_2 samples. The XPS peaks at 529.8 and 531.3 eV are the typical peaks of Ti–O–Ti and Ti–OH species [34–36], respectively. Deconvolution and curve fitting of the O 1s 2p spectra were performed by CasaXPS software, and the corresponding data are given in Table 1. It can be seen that the content of Ti–OH species in the H- TiO_2 sample is substantially higher than that in air- TiO_2 sample, indicating that the H- TiO_2 surfaces are functionalized by hydroxyl groups.

Fig. 5a and b shows the SEM images of the porous Ti film obtained by the dealloying. The Ti film exhibits a 3D nanoporous

Table 1
XPS data for O 1s.

Sample	Binding energy (eV)	Area (%)	Binding energy (eV)	Area (%)	Ti–OH%
H- TiO_2	529.31	70.42	531.59	29.58	29.58
Air- TiO_2	529.31	84.63	531.92	15.38	15.37

structure with open pores and interconnected nanoflakes that are nearly perpendicular to the substrate. In the dealloying process of the annealed Ti–Zn film in the alkaline solution, the more active zinc atoms are selectively dissolved, and the more noble titanium atoms are chemically driven to aggregate into two-dimensional (2D) nanoflakes by a phase separation process [37,39]. As illustrated by the top-view SEM images in Fig. 5c and d, the as-prepared H- TiO_2 film exhibits a 3D nanoporous network structure. The TEM images in Fig. 6a–c clearly show that the 3D nanoporous network film consists of many long TiO_2 nanotubes with an inner diameter of 5–10 nm and a wall thickness of 2–4 nm. The selected area electron diffraction (SAED) pattern in Fig. 6d shows the five sets of obvious diffraction rings that can be indexed as the A(101), R(110), A(112), A(200) and R(211) planes of TiO_2 from the inner to the outer, confirming that the as-prepared film is composed of anatase (A) and rutile (R) phases. As illustrated by the cross-sectional SEM image of H- TiO_2 film in the inset of Fig. 5c, the oriented TiO_2 nanotubes perpendicularly grow on Ti substrate, and the thickness of the H- TiO_2 film is about 1.5 μm . These long and thin TiO_2 nanotubes are prone to bend and enlance with each other, thus the top-view SEM images of as-prepared H- TiO_2 film exhibit a

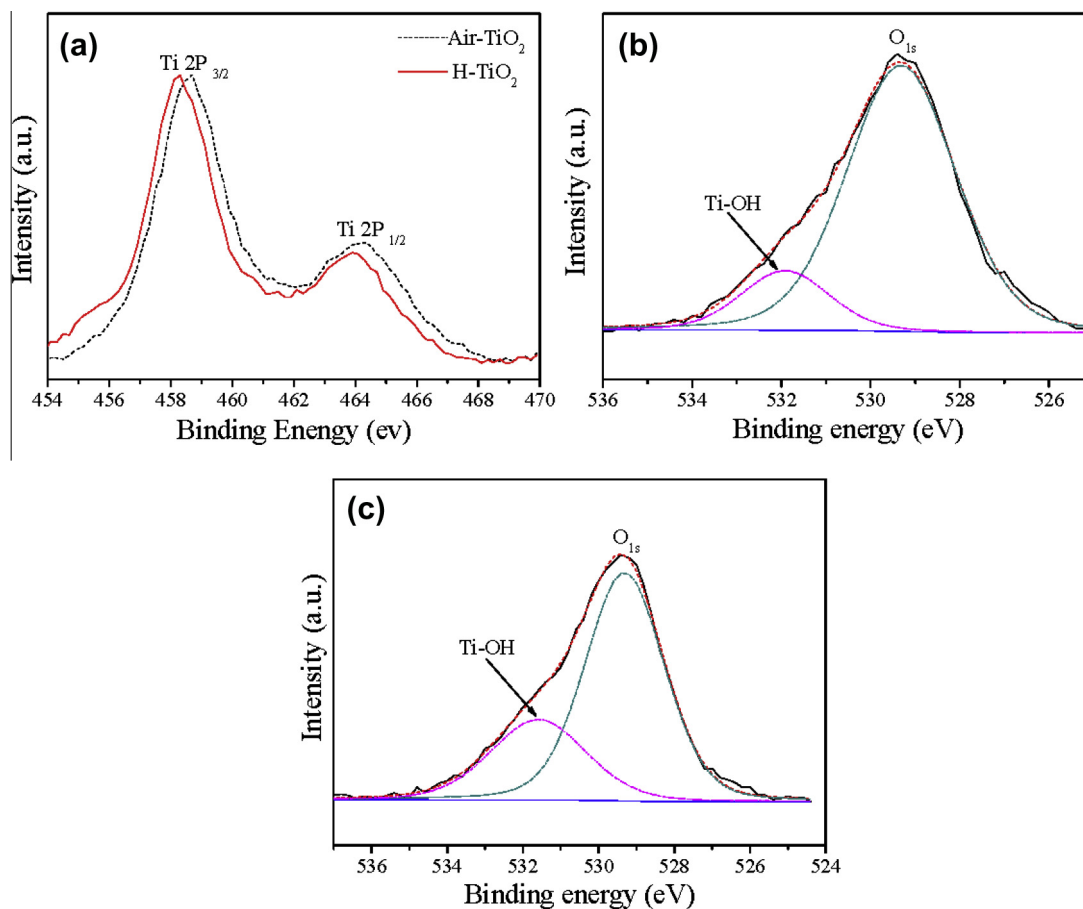


Fig. 4. XPS spectra of Ti 2p peaks (a) and O 1s peaks for Air- TiO_2 (b) and H- TiO_2 (c).

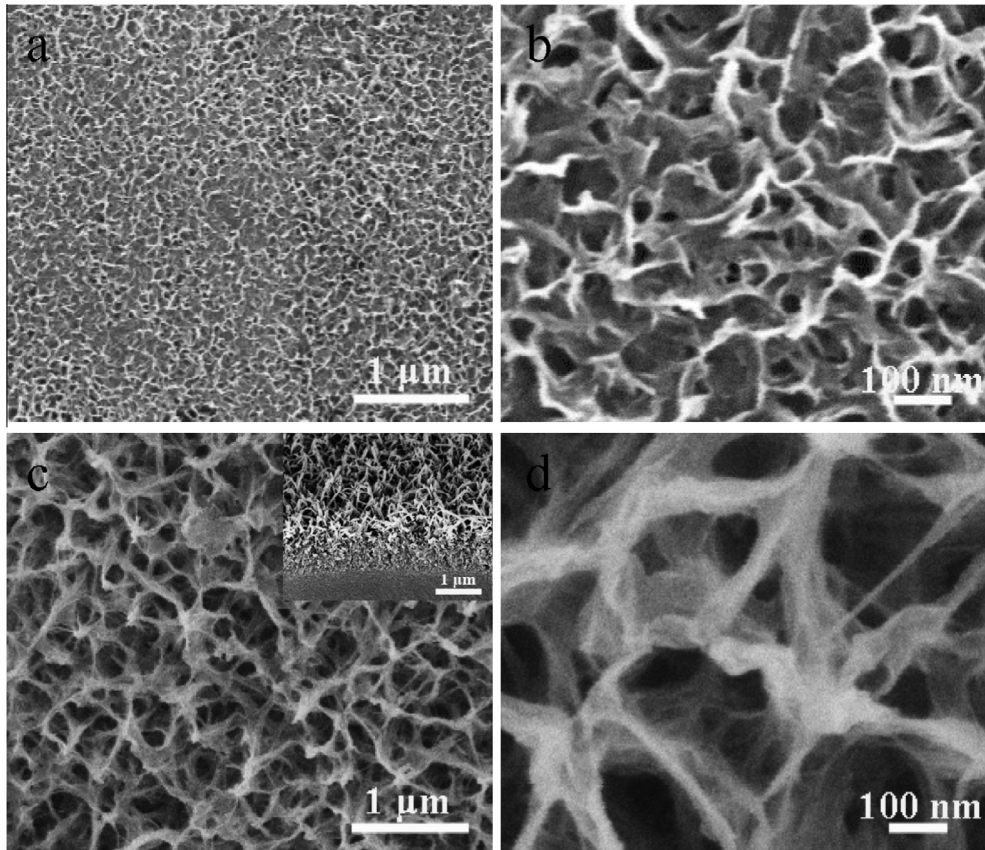


Fig. 5. SEM images of the porous Ti film obtained by dealloying (a, b) and H-TiO₂ film (c, d). The inset in c shows the cross-sectional SEM image of H-TiO₂ film.

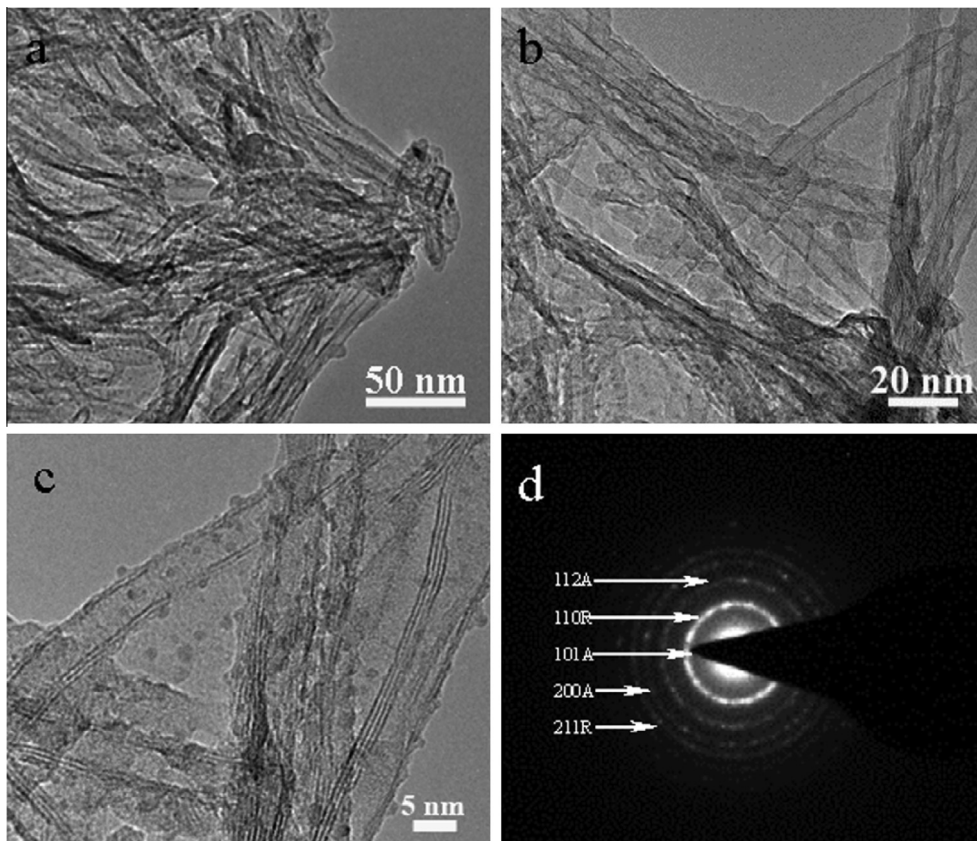


Fig. 6. TEM images (a–c) and SAED pattern (d) of H-TiO₂ network film. Symbols A and R in d represent anatase and rutile phases, respectively.

nanoporous network structure. That is, the as-prepared 3D nanoporous H-TiO₂ network film is formed by the interconnected TiO₂ nanotubes perpendicularly growing on Ti substrate. It should be pointed out that the transformation from the 2D titanium nanoflakes to the titania nanotubes could result from the oxidation of oxygen and a wrapping process during the alkali refluxing treatment [40,41]. The corresponding rolling-up mechanism involves the wrapping of multilayered nanosheets into nanotubes, where the driving force for the curving of multilayered nanosheets may be the mechanical stress induced during the oxidation/peeling of nanosheets [42].

Fig. 7a shows the cyclic voltammetric (CV) curves of the 3D nanoporous TiO₂ network films in 0.5 M Na₂SO₄ aqueous solution at the scan rate of 100 mV s⁻¹. The two CV curves exhibit nearly symmetrical rectangular shapes, indicative of electrical double-layer capacitance behavior. In comparison to the 3D air-TiO₂ network film, the 3D H-TiO₂ network film shows substantially larger capacitive current densities, suggesting its higher electrochemical activity. As illustrated in Fig. 7b, all the CV curves of the 3D H-TiO₂ network film at various scan rates exhibit quasi-rectangular shapes, and no significant change in the CV shapes appears as the scan rate increases from 2 to 1000 mV s⁻¹. This indicates the good capacitive behavior and high-rate capability of the 3D H-TiO₂ network film. Fig. 7c shows the calculated areal capacitances of the 3D nanoporous TiO₂ network films as a function of scanning rate. The areal capacitances of the 3D H-TiO₂ network film are much larger than the corresponding values of the 3D air-TiO₂ network film. For example, the 3D H-TiO₂ network film displays a capacitance of 1.05 mF cm⁻² at the scanning rate of 100 mV s⁻¹, which is a 14-fold enhancement compared to the air-TiO₂ film (0.07 mF cm⁻²). The areal capacitance of the H-TiO₂ network film is also substantially higher than those capacitance values recently

reported for TiO₂ electrodes [22–33,38]. Although our H-TiO₂ network film shows slightly lower areal capacitance value than the anodized TiO₂ nanotube array calcined in pure hydrogen gas [43], it is fabricated by a novel and controllable method, and its thermal treatment is conducted in the less hydrogen atmosphere. It is noted in Fig. 7c that the areal capacitance of the 3D H-TiO₂ network film drops from 1.21 to 0.70 mF cm⁻² when the scanning rate increases from 2 to 1000 mV s⁻¹, with a capacitance retention ratio of 58.0%. In comparison, the air-TiO₂ network film shows a capacitance retention ratio of 28.6%. This suggests that the 3D H-TiO₂ network film has an enhanced rate capability.

The electrochemical properties of the 3D nanoporous H-TiO₂ network film were further investigated by galvanostatic charge/discharge measurements. Fig. 8a exhibits the charge/discharge curves of different TiO₂ film electrodes at the current density of 100 μ A cm⁻². Compared with those of the pristine-TiO₂ and air-TiO₂ film electrodes, the charge/discharge curves of the H-TiO₂ film electrode are substantially prolonged, revealing an enhanced capacitive behavior. The areal capacitance of the H-TiO₂ film electrode is calculated to be 0.89 mF cm⁻², which is significantly larger than the corresponding values of the pristine-TiO₂ (0.06 mF cm⁻²), air-TiO₂ (0.12 mF cm⁻²) and the previously reported TiO₂ electrodes [22–33]. Fig. 8b shows the charge/discharge curves of the H-TiO₂ network film electrode at the current densities ranging from 100–1000 μ A cm⁻². It can be seen that the charge curves are clearly symmetrical to their corresponding discharge counterparts, and the charge/discharge potentials linearly vary with time. This shows the non-faradaic capacitance behavior and good rate capability of the 3D H-TiO₂ network film, which is in good agreement with the CV results. Fig. 8c presents the cycle performance of the pristine-TiO₂, Air-TiO₂ and H-TiO₂ network film electrodes at the current density of 100 μ A cm⁻². The H-TiO₂ network film

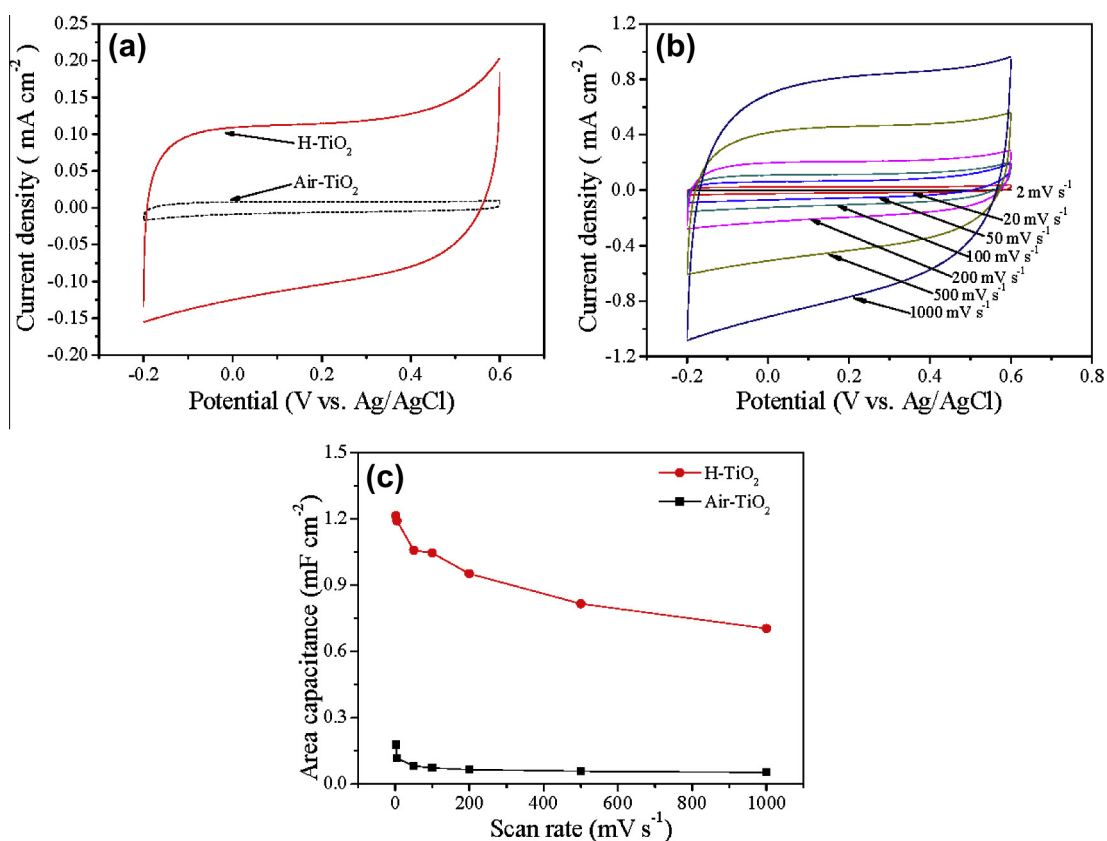


Fig. 7. (a) CV curves of the H-TiO₂ and air-TiO₂ network films obtained at a scanning rate of 100 mV s⁻¹. (b) CV curves collected for the H-TiO₂ network film at various scan rates. (c) Areal capacitance of H-TiO₂ and air-TiO₂ network films measured as a function of scan rate.

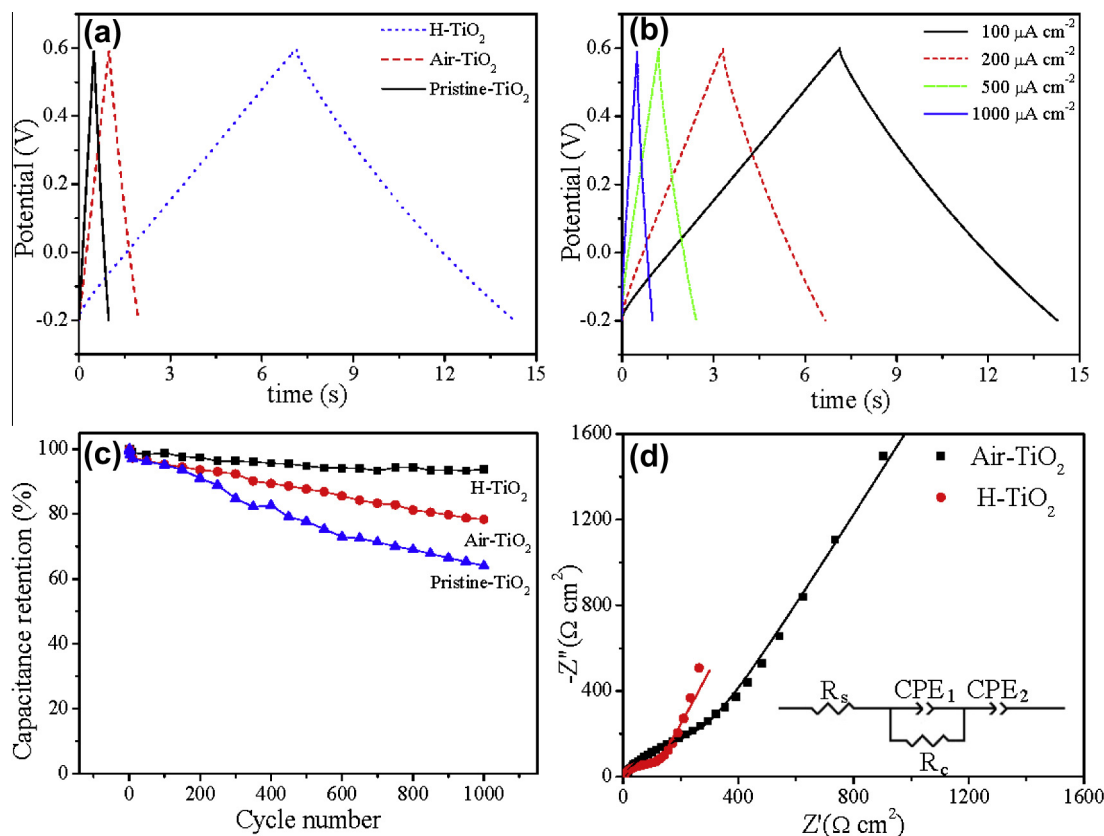


Fig. 8. (a) Galvanostatic charge–discharge curves of pristine-TiO₂, air-TiO₂ and H-TiO₂ network films collected at a current density of 100 $\mu\text{A cm}^{-2}$. (b) Galvanostatic charge–discharge curves of H-TiO₂ network film collected at current densities of 100–1000 $\mu\text{A cm}^{-2}$. (c) Cycle performance of pristine-TiO₂, air-TiO₂ and H-TiO₂ network films at a current density of 100 $\mu\text{A cm}^{-2}$. (d) Nyquist plots for air-TiO₂ and H-TiO₂ film electrodes at open circuit state and the corresponding equivalent circuit in the inset.

electrode exhibits only 6.2% deterioration of the initial capacitance after 1000 cycles. While the capacitance losses of the pristine-TiO₂ and Air-TiO₂ film electrodes after 1000 cycles are 35.96% and 21.63%, respectively. This demonstrates the enhanced electrochemical cycling performance of the H-TiO₂ network film electrode.

The EIS measurements were performed to evaluate the effects of hydrogenation on the electrochemical kinetics of the 3D TiO₂ network films. Fig. 8d shows the Nyquist plots for the electrodes at open circuit state. The Nyquist plots of the two samples display a similar shape. Considering that no evidence of any faradaic reaction is observed in both the CV and charge/discharge curves, it is reasonable to conclude that the depressed semicircle in the high-frequency region can be attributed to the contact resistance (R_c) and capacitance (CPE1) between the TiO₂ nanotubes and titanium substrate [44]. In the low-frequency region, the imaginary part of the impedance is much larger than the corresponding real part, which is a characteristic of the capacitive behavior [45,46]. The loop in the low-frequency region is related to the double-layer capacitance (CPE2). The equivalent circuit of the EIS is shown in the inset of Fig. 8d, where R_s is the bulk solution resistance [44–47]. It can be seen from the simulation results in Table 2 that the H-TiO₂ network film shows a much lower contact resistance (R_c) and a much larger double-layer capacitance (CPE2) value compared to the air-TiO₂ network film. This implies that the electrical conductivity and double-layer capacitance of the 3D TiO₂ network film are effectively improved by the hydrogenation treatment.

The excellent electrochemical capacitance properties of the as-prepared 3D nanoporous H-TiO₂ network film electrode can be attributed to its unique structure characteristics. The hierarchically nanoporous architecture assembled from long and thin TiO₂ nanotubes not only provides easy access of the surfaces to liquid elec-

Table 2

Parameter values obtained by the simulation of the Nyquist plots in Fig. 8d.

Sample	R_s ($\Omega \text{ cm}^2$)	R_c ($\Omega \text{ cm}^2$)	CPE1 ($\mu\text{F cm}^{-2}$)	n_1	CPE2 ($\mu\text{F cm}^{-2}$)	n_2
H-TiO ₂	3.32	101.30	31.60	0.87	465.9	0.76
Air-TiO ₂	4.97	231.60	13.38	0.78	60.96	0.72

trolyte but also offers more active sites for the charge separation, manifesting the larger specific capacitance. Hydrogenation leads to the occurrence of Ti³⁺ (oxygen vacancies) in H-TiO₂ phase and the formation of more hydroxyl groups on the surface of H-TiO₂ nanotubes, which improves electrical conductivity and increases the active sites for the adsorption/desorption of ions [36]. This is largely responsible for the excellent capacitance performance of the H-TiO₂ network film electrode, especially at a high current rate. The titania nanotubes are in-situ formed by using the 2D titanium nanoflakes as precursor, thus they have the robust adhesion on the substrate, which could play an important role in ensuring the enhanced rate capability and excellent electrochemical cycling stability of the H-TiO₂ network film electrode. Different from the TiO₂ nanotube arrays in the previous investigations [28,29,31,33], the 3D H-TiO₂ network film in this work is composed of the interconnected long and thin TiO₂ nanotubes perpendicularly growing on Ti substrate, thereby facilitating the transport of electrons. This has certain contribution to the enhanced capacitance performance of the H-TiO₂ network film electrode.

4. Conclusions

The 3D nanoporous hydrogenated TiO₂ network film on titanium substrate has been successfully fabricated by the novel

strategy involving dealloying, alkali reflux and hydrogenation. The 3D H-TiO₂ network film consists of the interconnected long and thin TiO₂ nanotubes resulting from the oxidation of the 2D titanium nanoflakes obtained by the dealloying. Hydrogenation results in the formation of oxygen vacancies in H-TiO₂ phase and more hydroxyl groups on the surface of H-TiO₂ nanotubes, which increases the electrical conductivity and the active sites for the adsorption/desorption of ions. The 3D nanoporous H-TiO₂ network film exhibits the substantially large specific capacitance, enhanced rate capability and excellent electrochemical cycling performance. This results from the hierarchically nanoporous network architecture, the formation of oxygen vacancies and more hydroxyl groups, and the robust adhesion on titanium substrate. These attractive results are important for both developing the novel fabrication strategy of the 3D nanostructured film and promoting the promising applications of TiO₂ materials in some energy storage and conversion systems such as supercapacitors and Li-ion batteries.

Acknowledgements

This work was supported by the National Natural Science Foundation of China (Nos. 51174176, 51271168 and J1210042) and the Specialized Research Fund for the Doctoral Program of Higher Education of China (Grant No. 20120101110045).

References

- [1] J. Miller, P. Simon, *Science* 321 (2008) 651–652.
- [2] P. Simon, Y. Gogotsi, *Nat. Mater.* 7 (2008) 845–854.
- [3] G.P. Wang, L. Zhang, J.J. Zhang, *Chem. Soc. Rev.* 41 (2012) 797–828.
- [4] R.R. Salunkhe, K. Jang, H. Yu, S. Yu, T. Ganesh, S.H. Han, H. Ahn, *J. Alloys Comp.* 509 (2011) 6677–6682.
- [5] L.Y. Niu, Z.P. Li, J.F. Sun, Z.J. Fan, Y. Xu, P.W. Gong, S.R. Yang, J.Q. Wang, *J. Alloys Comp.* 575 (2013) 152–157.
- [6] K.V. Gurav, U.M. Patil, S.W. Shin, G.L. Agawane, M.P. Suryawanshi, S.M. Pawar, P.S. Patil, C.D. Lokhande, J.H. Kim, *J. Alloys Comp.* 573 (2013) 27–31.
- [7] Y. Chen, X. Zhang, D.C. Zhang, P. Yu, Y.W. Ma, *Carbon* 49 (2011) 573–580.
- [8] D.P. Dubal, S.V. Patil, A.D. Jagadale, C.D. Lokhande, *J. Alloys Comp.* 509 (2011) 8183–8188.
- [9] S. Chen, J.W. Zhu, X.D. Wu, Q.F. Han, X. Wang, *ACS Nano* 4 (2010) 2822–2830.
- [10] Y.H. Xu, J.C. Guo, C.S. Wang, *J. Mater. Chem.* 22 (2012) 9562–9567.
- [11] L.Y. Zhang, Y. Zhong, Z.S. He, J.M. Wang, J. Xu, J. Cai, N. Zhang, H. Zhou, H.Q. Fan, H.B. Shao, J.Q. Zhang, C.N. Cao, *J. Mater. Chem. A* 1 (2013) 4277–4285.
- [12] D.W. Kim, K.Y. Rhee, S.J. Park, *J. Alloys Comp.* 530 (2012) 6–10.
- [13] L.Y. Zhang, L. Xu, J.M. Wang, H.B. Shao, Y.Q. Fan, J.Q. Zhang, *J. Phys. Chem. C* 115 (2011) 18027–18034.
- [14] P. Acevedo-Pena, L. Lartundo-Rojas, I. Gonzalez, *J. Electrochem. Soc.* 160 (2013) C291–C297.
- [15] C. Wang, D.L. Wang, C.S. Dai, *J. Electrochem. Soc.* 155 (2008) A390–A394.
- [16] L.Y. Liang, H.M. Liu, W.S. Yang, *J. Alloys Comp.* 559 (2013) 167–173.
- [17] Z.X. Song, W. Liu, M. Zhao, Y.J. Zhang, G.C. Liu, C. Yu, J.S. Qiu, *J. Alloys Comp.* 560 (2013) 151–155.
- [18] M.X. Liao, Y.F. Liu, Z.H. Hu, Q. Yu, *J. Alloys Comp.* 562 (2013) 106–110.
- [19] K. Brezesinski, J. Wang, J. Haetge, C. Reitz, S.O. Steinmueller, S.H. Tolbert, B.M. Smarsly, B. Dunn, T. Brezesinski, *J. Am. Chem. Soc.* 132 (2010) 6982–6990.
- [20] D.S. Kong, J.M. Wang, H.B. Shao, J.Q. Zhang, C.N. Cao, *J. Alloys Comp.* 509 (2011) 5611–5616.
- [21] J.M. Macak, F. Schmidt-Stein, P. Schmuki, *Electrochem. Commun.* 9 (2007) 1783–1787.
- [22] F. Fabregat-Santiago, H. Randriamahazaka, H. Randriamahazaka, A. Zaban, J. Garcia-Canadas, G. Garcia-Belmonte, J. Bisquert, *Phys. Chem. Chem. Phys.* 8 (2006) 1827–1833.
- [23] D. Dambournet, I. Belharouak, K. Amine, *Chem. Mater.* 22 (2010) 1173–1179.
- [24] Y.B. Xie, L.M. Zhou, C.J. Huang, H.T. Huang, J. Lu, *Electrochim. Acta* 53 (2008) 3643–3649.
- [25] T. Brezesinski, J. Wang, S.H. Tolbert, B. Dunn, *J. Sol-Gel. Sci. Technol.* 57 (2011) 330–335.
- [26] B.E. Conway, W.G. Pell, *J. Solid State Electrochem.* 7 (2003) 637–644.
- [27] A. Ramadoss, S.J. Kim, *J. Alloys Comp.* 561 (2013) 262–267.
- [28] M. Salari, K. Konstantinov, H.K. Liu, *J. Mater. Chem.* 21 (2011) 5128–5133.
- [29] Z. Endut, M. Hamdi, W.J. Basirun, *Appl. Surf. Sci.* 280 (2013) 962–964.
- [30] Z.Y. Zhang, F. Xiao, Y.L. Guo, S. Wang, Y.Q. Liu, *ACS Appl. Mater. Inter.* 5 (2013) 2227–2233.
- [31] M.S. Kim, T.W. Lee, J.H. Park, *J. Electrochem. Soc.* 156 (2009) A584–A588.
- [32] J. Wang, J. Polleux, J. Lim, B. Dunn, *J. Phys. Chem. C* 111 (2007) 14925–14931.
- [33] M. Salari, S.H. Aboutalebi, K. Konstantinov, H.K. Liu, *Phys. Chem. Chem. Phys.* 13 (2011) 5038–5041.
- [34] X.B. Chen, L. Liu, P.Y. Yu, S.S. Mao, *Science* 331 (2011) 746–750.
- [35] M.S. Lazarus, T.K. Sham, *Chem. Phys. Lett.* 92 (1982) 670–674.
- [36] A. Naldoni, M. Allieta, S. Santangelo, M. Marelli, F. Fabbri, S. Cappelli, C.L. Bianchi, R. Psaro, V.D. Santo, *J. Am. Chem. Soc.* 134 (2012) 7600–7603.
- [37] J. Cai, J. Xu, J.M. Wang, L.Y. Zhang, H. Zhou, Y. Zhong, D. Chen, H.Q. Fan, H.B. Shao, J.Q. Zhang, C.N. Cao, *Int. J. Hydrogen Energy* 38 (2013) 934–941.
- [38] M. Koelsch, S. Cassaignon, C.T.T. Minh, J.F. Guillemoles, J.P. Jolivet, *Thin Solid Films* 451 (2004) 86–92.
- [39] J. Erlebacher, M.J. Aziz, A. Karma, N. Dimitrov, K. Sieradzki, *Nature* 410 (2001) 450–453.
- [40] D.V. Bavykin, V.N. Parmon, A.A. Lapkin, F.C. Walsh, *J. Mater. Chem.* 14 (2004) 3370–3377.
- [41] A. Kukovec, N. Hodos, E. Horvath, G. Radnoczi, Z. Konya, I. Kiricsi, *J. Phys. Chem. B* 109 (2005) 17781–17783.
- [42] D. Wu, J. Liu, X.N. Zhao, A.D. Li, Y.F. Chen, N.B. Ming, *Chem. Mater.* 18 (2006) 547–553.
- [43] X.H. Lu, G.M. Wang, T. Zhai, M.H. Yu, J.Y. Gan, Y.X. Tong, Y. Li, *Nano Lett.* 12 (2012) 1690–1696.
- [44] H.H. Lee, K.Y. Lee, J.Y. Lee, *J. Alloys Comp.* 260 (1997) 201–207.
- [45] Y. Liu, R. Zhao, M. Ghaffari, J.H. Lin, S. Liu, H. Cebeci, R.G. Villoria, R. Montazami, D. Wang, B.L. Wardle, J.R. Heflin, Q.M. Zhang, *Sens. Actuat. A-Phys.* 181 (2012) 70–76.
- [46] X.M. Liu, L. Juan, L. Zhan, L. Tang, Y.L. Wang, W.M. Qiao, X.Y. Liang, L.C. Ling, *J. Electroanal. Chem.* 642 (2010) 75–81.
- [47] F. Gopal, M. Faraji, *Electrochim. Acta* 100 (2013) 133–139.